

Partial Surface Selenization of Cobalt Sulfide Microspheres for Enhancing the Hydrogen Evolution Reaction

Biswanath Dutta,^{1,‡} Yang Wu,^{2,‡} Jie Chen,³ Jin Wang,³ Junkai He,² Mohamed Sharafeldin,^{1,4} Peter Kerns,¹ Lei Jin,¹ Avinash M. Dongare,³ James Rusling,^{1,2,5,6} Steven L. Suib^{1,2,*}

¹ Department of Chemistry, University of Connecticut, 55 North Eagleville Road, Storrs, CT 06269, USA.

² Institute of Material Science, University of Connecticut, 97 North Eagleville Road, Storrs, CT 06269, USA.

³ Department of Material Science and Engineering, University of Connecticut, 97 North Eagleville Road, Storrs, CT 06269, USA.

⁴ Analytical Chemistry Department, Zagazig University, Zagazig, Egypt.

⁵ Department of Surgery and Neag Cancer Center, University of Connecticut Health Center, Farmington, CT, USA

⁶ School of Chemistry, National University of Ireland, Galway, Galway, Ireland

ABSTRACT: Electrocatalysis of water is a scalable and easily available source of the production of hydrogen (H₂), the future energy carrier. This drive for clean energy inspired us to develop an inexpensive, readily producible, highly active, and stable catalyst to replace current state of the art platinum catalysts. Building on the promising hydrogen evolution reaction (HER) activity of many pyrites, their structural tuning by different metal/non-metals has been found to be effective in several instances. We present here one such effort by partial surface selenization of mesoporous cobalt sulfide material which displayed long-term operational stability (for at least 25 hours) besides attaining a current density of 100 mA cm⁻² at an overpotential of 160 mV versus the reversible hydrogen electrode (RHE) (in acidic media). A low Tafel slope (of 52 mV dec⁻¹) and high exchange current density (*j*₀) (of 70 μA cm⁻²) make our catalyst better to most existing systems. More importantly, using a variety of analytical techniques, electrochemical measurements, and theoretical calculations, we have analyzed the morphology of the material, and rationalized the key to the enhanced intrinsic activity (as compared to the meso-CoS₂) per active site. This study is expected to explain similar systems and modify approaches to enhancing the electrochemical activity of metal chalcogenides.

Keywords: Cobalt sulfide, selenide, sulfoselenide, hydrogen evolution reaction, electrocatalysis, Gibbs free energy.

The electrochemical hydrogen evolution reaction (HER) from water is believed to be the cleanest and most sustainable approach for hydrogen (H₂) production to meet future terawatt energy demands.^{1,2} To produce hydrogen in a facile way for industrial applications, a highly active and robust catalyst is required which minimizes the energy barrier, here represented by the overpotential (η) of this process.³ To date, platinum (Pt) and its alloys are considered to be the most active HER catalysts due to their high stability and lowest overpotential (~25-35 mV of overpotential to achieve a geometrical current density of 10 mA

cm⁻²).⁴ However, the scarcity and high cost of platinum (Pt) limit its widespread application.^{5,6} Hence, to replace platinum (Pt), the development of a highly active (close to Pt), sustainable, and cost-effective catalyst is in urgent need. Inspired by this rising demand, scientists across the world have started exploring possibilities of developing a hydrogen economy. This has led to various binary (such as metal oxides,^{7,8} nitrides,⁹ sulfides,¹⁰⁻²⁶ selenides,²⁷⁻³¹ phosphides,³²⁻³⁶ carbides,^{9,37} and borides.³⁷) and ternary transition metal compounds (such as MoPS,³⁸ WPS,³⁹ CoPS,⁴⁰ WSSe,³⁹ MoSSe-NiSe₂,⁴¹ and bimetallic alloys.⁴²⁻⁴⁴) as HER

catalysts. Among them, pyrite-type transition metal dichalcogenides (MX_2 , where $\text{M} = \text{Fe}, \text{Co}$, or Ni and $\text{X} = \text{O}, \text{S}$ or Se) have gained significant attention due to their high natural abundance, excellent stability (under both acidic and basic solutions), and outstanding HER performance, which makes them attractive for industrial applications.⁴⁵

enhanced activity of rarely studied selenium doped metal pyrites, we initiated investigations. Herein, we demonstrate the synthetic route of a unique surface selenized mesoporous cobalt sulfide electrocatalyst, its excellent HER activity, chemical stability, and the determination of its surface active sites. Formation of these active sites and their effects were evaluated by

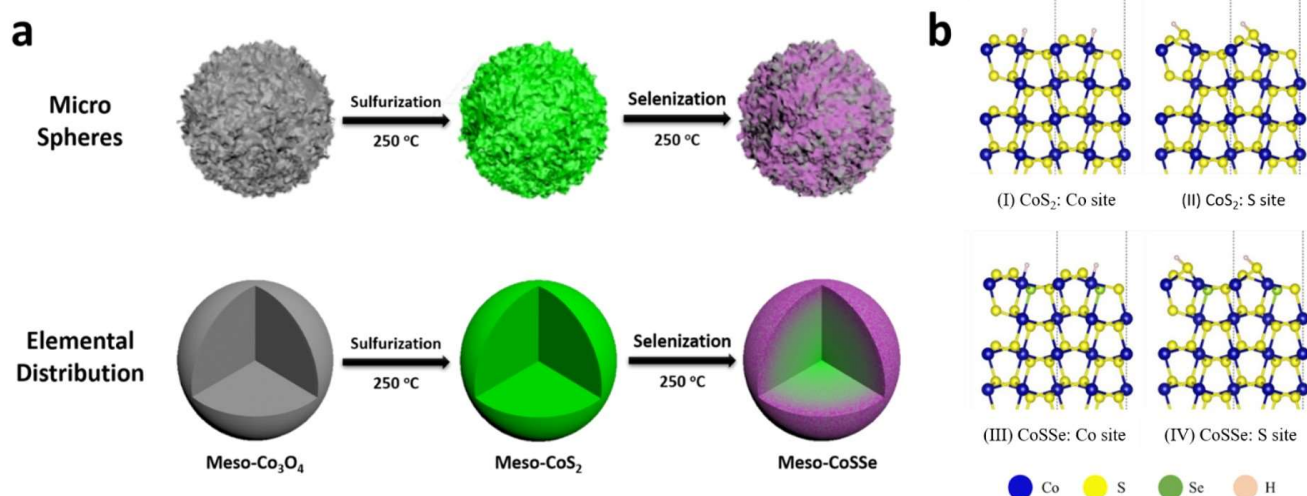


Figure 1. a) Schematic representation of the catalyst synthesis, b) Schematic structural representations for H adsorption on {001} different surface elements: (I) on Co of CoS_2 , (II) on S of CoS_2 , (III) on Co of CoSSe , and (IV) on S of CoSSe .

Transition metal pyrites are also known for various energy-related applications due to their metallic and semiconducting properties.⁴⁶ However, in HER the electron donating property of chalcogenides is suggested to be a primary requirement.⁴⁰ This requires the tuning of the electronic feature of X_2^{2-} dumbbells in metal pyrites by varying the atomic ratio of elements, which is considered to be highly crucial to enhancing the hydrogen adsorption process.⁴⁷ A recent study on cobalt phosphosulfide (CoPS) has successfully showcased how the replacement of sulfur by phosphorus tune the electronic structure of the catalyst to aid the hydrogen evolution reaction.⁴⁰ Followed by this, various selenium doped or alloyed ternary metal pyrites such as $\text{WS}_{2(1-x)}\text{Se}_{2x}$, $\text{CoS}_{2(1-x)}\text{Se}_{2x}$, and $\text{MoS}_{2(1-x)}\text{Se}_{2x}$ were prepared, which exhibited excellent enhancement of HER activity compared to WS_2 and MoS_2 , respectively.^{39,44-46} In CoPS , phosphorous (P) doping converted S_2^{2-} to $(\text{SP})^{3-}$ dumbbells.⁴⁰ This was shown to increase the surface electron density of the material which caused better adsorption of thermoneutral hydrogens. However, this enhancement of the negative charge of the anionic site is not possible in the selenium doped system, as the electronic nature of sulfur and selenium are comparable. Therefore, in the rush of unraveling the source of

electrochemical impedance spectroscopy (EIS), X-ray photoelectron spectroscopic (XPS) techniques, and active site blocking experiments. Moreover, a Density Functional Theory (DFT) computed study was used to support the stability of the material and our experimental findings.

Since electrochemical HER is a surface phenomenon, it has been reported to be highly dependent on the surface area of a material which is a direct measure of the number of active sites.⁵¹ This makes materials with a higher number of active sites of great interest. An increase in the number of active sites is believed to contribute towards the higher catalytic efficiency of materials by raising their rate of charge transfer and product diffusion.⁵¹ This led us to develop mesoporous cobalt sulfide and sulfoselenide materials, as mesopores are known to increase the surface area of a material. Consequently, a simple three-step synthetic protocol was implemented. This involved the synthesis of mesoporous cobalt oxide ($\text{meso-Co}_3\text{O}_4$) material by a soft template mediated solvent evaporation induced self-assembly method, developed by our group,⁵² followed by its sulfurization to produce meso-CoS_2 . Finally, a controlled selenization of this meso-CoS_2 material (at 250°C for 12 hours) yielded the partially surface selenized meso-CoSSe-12h catalyst. The schematic

representation of the synthetic protocol of these catalysts is shown in **Fig. 1. a** and thoroughly described in the methods section.

To comprehend the stability of the enlarged lattice structure of meso-CoS₂-12h, we compared the total energies of both meso-CoS₂ and meso-CoS₂-12h. Hence, lattice structures of CoS₂ and CoS₂-12h were modeled using Density Functional Theory (DFT) calculations, assuming ~25 % of surface selenium (**Fig. 1. b. III, and IV**) based on the SEM-EDX mapping, as mentioned later.

The surface morphology of resulting meso-CoS₂-12h catalyst was analyzed by multiple characterization techniques. To learn about the crystal structure of this material, powder X-ray diffraction (PXRD) was measured and compared with meso-CoS₂ (**Fig. 2. a**). The PXRD pattern of meso-CoS₂-12h was indexed as a sulfur-deficient pyrite (CoS₂) system, identical with that of meso-CoS₂ (space group *Pa-3*, *a* = 5.5385 Å, ICSD collection code #86351). Nevertheless, a minor increment (of 0.0108 Å) of lattice constant (*a* = 5.5493 Å) was observed for meso-CoS₂-12h as compared to the meso-CoS₂ (**Fig. 2. b**), depicting a small expansion of the unit cell. This could be due to the larger ionic radii of selenium than sulfur. Interestingly, this 0.2 % strain, accumulated during the 0.0108 Å elongation of lattice constant upon selenium (Se) doping reflected a sudden drop in total energy (**Fig. S1. a**). A further increment of lattice strain of the system predicted an increase of the total energy, which supports the maximum stability of the system at 0.2 % strain (**Fig. S1. a**).

Confocal micro-Raman spectra (**Fig. S1. b**) of meso-CoS₂ displayed all five Raman active modes E_g (~295 cm⁻¹), T_g (1) (~330 cm⁻¹), A_g (~395 cm⁻¹), T_g (2) (~420 cm⁻¹) and T_g (3) (~490 cm⁻¹). Here, the A_g and T_g (2) modes correspond to the in-phase and out of phase stretching vibrations of sulfide (S₂²⁻) dumbbells of the pyrite lattice. E_g is the pure librational mode of the same, and T_g (1), T_g (3) modes are combinations of both stretching and librational vibrations.⁵³ Interestingly, all these modes were observed to be redshifted for meso-CoS₂-12h as compared to meso-CoS₂ (**Fig. S1. b**). This is attributed to a larger unit cell for meso-CoS₂-12h than meso-CoS₂, validating our earlier findings from X-ray diffraction studies. More importantly, the presence of one set of these

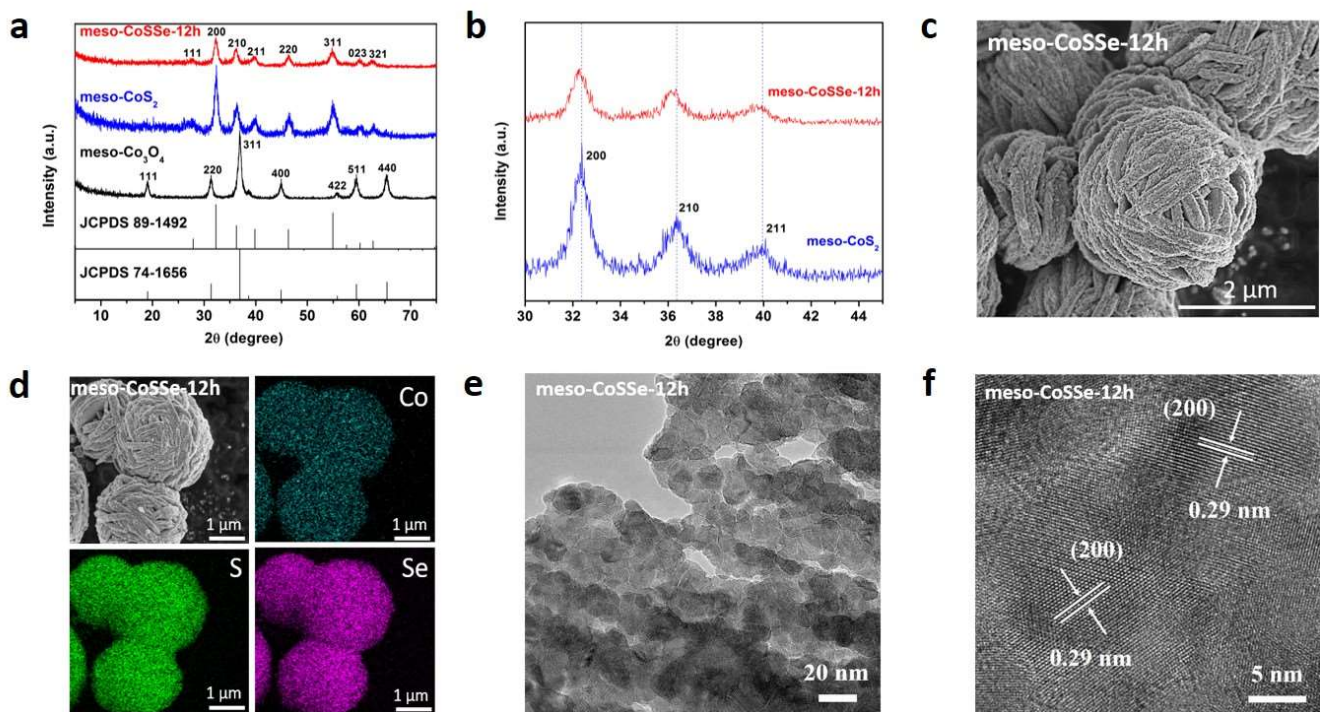


Figure 2. Morphology characterization. a) Wide angle Powder X-ray diffraction pattern (PXRD) of meso-Co₃O₄, meso-CoS₂, meso-CoSSe-12h catalyst, the JCPDS pattern for CoS₂, and the JCPDS pattern for Co₃O₄. b) Close up view of PXRD patterns of meso-CoS₂, and measure the XRD shift. c) SEM image of meso-CoSSe-12h catalysts. Scale bar, 2 μ m. d) SEM-EDX of meso-CoSSe-12h catalyst. e) HR-TEM image of meso-CoSSe-12h cat-

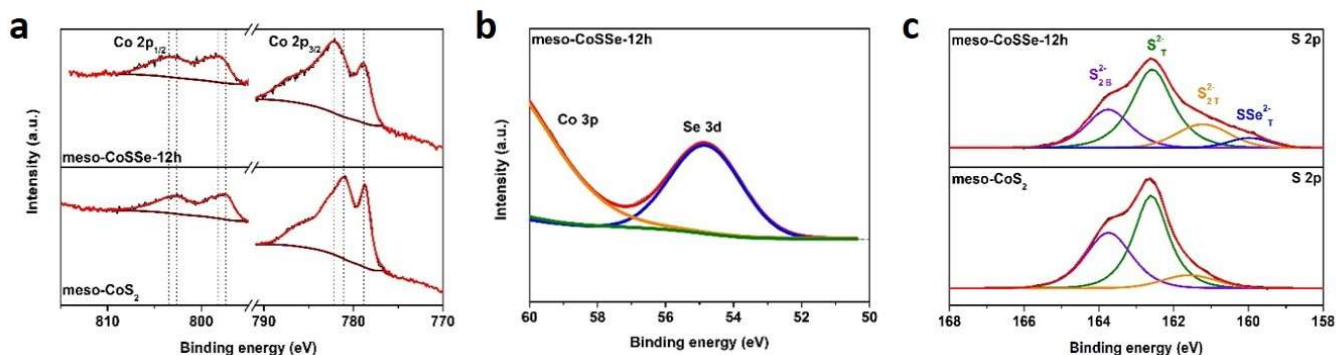


Figure 3. Characterization on the meso-CoSSe-12h. a) XPS spectra of Co 2p of meso-CoS₂, and meso-CoSSe-12h b) XPS spectra of Se 3d of meso-CoSSe-12h. c) XPS spectra of S 2p in meso-CoSSe-12h showing the effect of Se on the surface of meso-CoS₂.

(A_g, E_g, and T_g) peaks suggested that the surface of meso-CoSSe-12h has a single uniform phase rather than a binary mixture of two different solid phases.

Scanning electron microscopy (SEM; **Fig. 2. c.**) revealed the structural morphology of meso-CoSSe-12h which was similar to cabbage-like layered nanospheres of meso-CoS₂ (**Fig. S2. a**). Transmission electron microscopy was used to capture further details of these materials which revealed the presence of mesopores in both CoS₂ and CoSSe-12h catalysts (**Fig. 2. e**, and **Fig. S2. b**).

Larger ionic radii of selenium (Se) as compared to sulfur (S) probably expanded the unit cells in meso-CoSSe-12h, which decreased the surface area and porosity (**Fig. S3. a**). Barrett-Joyner-Halenda (BJH) pore size distribution methods, used to measure pore sizes, also detected this decrease of pore diameter upon selenization (**Fig. S3. b**). To determine the uniformity of selenium in meso-CoSSe, high-resolution transmission electron microscopy (HR-TEM) of meso-CoSSe-12h was analyzed. These experiments showed the presence of similar lattice fringes at

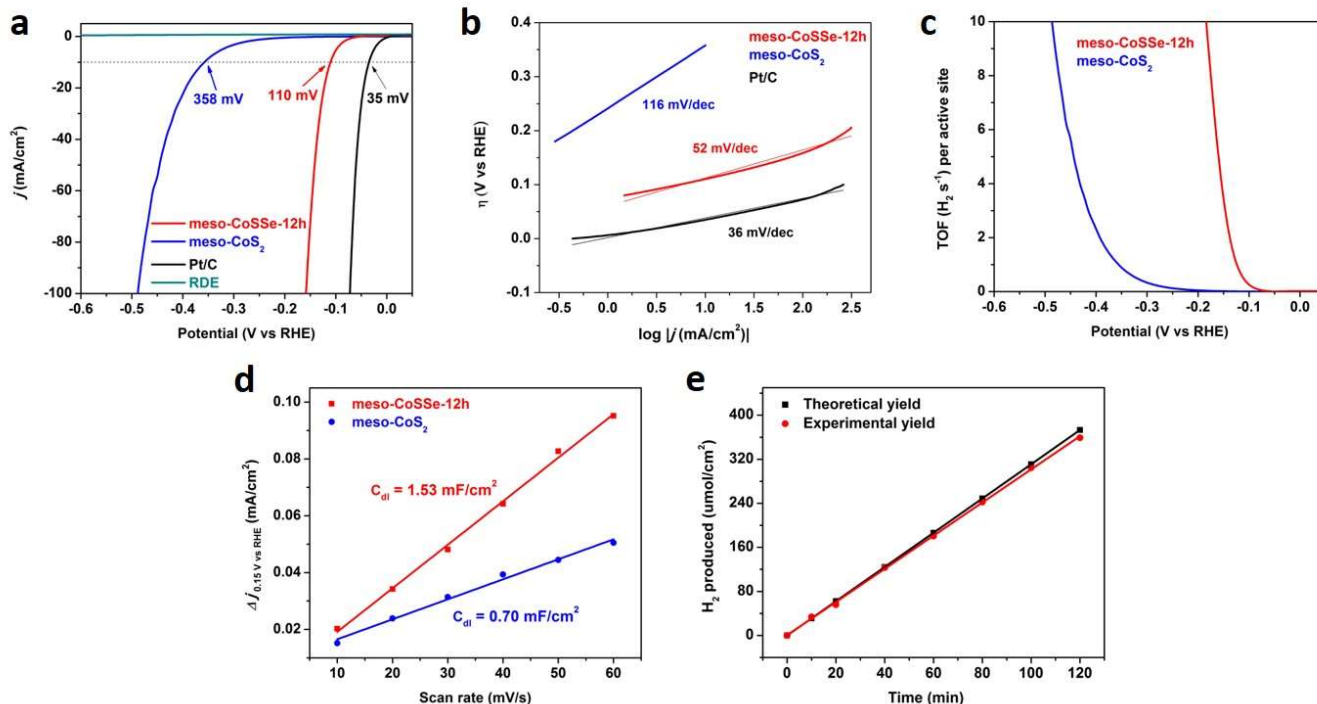
different areas. The elemental uniformity of Co, S, and Se in the meso-CoSSe-12h surface was further confirmed by SEM-EDX analysis as depicted in **Fig. 2. d**.

To further understand the details of the surface properties of meso-CoSSe-12h, XPS was utilized. An increase in binding energy of Co 2p in meso-CoSSe-12h as compared to meso-CoS₂ (**Fig. 3. a**), was observed which implies the oxidation of Co. A decrease in the percentage of metallic Co (Co⁰) (XPS peak at 778 eV) (**Fig. 3. a**) further supported this phenomenon. Unlike the oxidation of cobalt (Co), a comparison of the 2p region of sulfur (S) displayed reduction upon selenization of meso-CoS₂. The expansion of the 2p peak towards lower binding energy was assumed to happen due to the formation of a new species. To understand this, the S 2p regions of both materials were deconvoluted (**Fig. 3. c**) and compared. This analysis shows formation of a new terminal sulfur-selenium species (denoted as SSe²⁻) in meso-CoSSe-12h, besides the two-pre-existing bridged (S²⁻ and S₂²⁻) and one terminal sulfur species. In the meso-CoSSe-12h catalyst only one type of selenium species (present as selenide in the material) was found to form as revealed by the single peak at 54.8 eV (**Fig. 3. b**). This supports the homogeneity of sulfur and selenium moieties on the catalyst surface. More importantly, the generation of this

new sulfur species at lowest bind energy indicates the weakening of Co-S bonds and further supports the oxidation of Co (**Fig. 3. a**). Moreover, to know the surface composition of the material, SEM-EDX mapping was used, which yielded an empirical formula of CoS_{1.32}Se_{0.67} (**Fig. 2. d, and Table S1**). This further supported the presence of all three elements (Co, S, and Se) on the surface of the material. The aforementioned empirical formula was very close to that of the DFT computed model of meso-CoSSe (**Fig. 1. b, CoS_{1.5}Se_{0.5}**).

To further support this finding, the overall percentage of each element was measured using X-ray fluorescence (XRF) spectrometry, where the catalyst was digested by a mixture of HNO₃, HCl, and HF (9: 3: 8). XRF was used to detect the atomic ratio of different elements, to be 27 % of Co, 54 % for S, and 18 % for Se with an error bar of 0.5 % (**Table S1**). Consequently, this generated an empirical formula of Co₂Se_{0.67}. The comparison between the empirical formulas generated by XPS and XRF validates the presence of a higher percentage of Se on the surface of meso-CoSSe. This supports our prior assumption of surface selenization.

The percentages of surface elements (Co, S, and Se) were controlled by varying the selenization time (summarized in **Table S1**). Thus, to investigate the effect of Se content on meso-CoS₂,



layer capacitance (C_{dl}) for meso-CoS₂ and meso-CoSSe-12h electrodes. (c) Hydrogen amount from theoretical calculations (black square) and experimental tests (red sphere) vs. time for the meso-CoSSe-12h catalyst at -20 mA for 120 min. The straight line represents the theoretically calculated amounts of H₂ assuming 100 % Faradaic efficiency, and the scattered dots represent the point where produced H₂ were measured by gas chro-

meso-CoS₂ catalysts with different amounts of Se were evaluated using their polarization (LSV) curves. A continuous increase of HER activity with increasing Se content was observed. However, instead of obtaining a linear plot, a Gaussian curve with a saturation point at 12 hours was obtained (**Fig. S5. a**). Tafel slopes of these materials also showed similar Gaussian curves with a saturation point at 12 hours (**Fig. S5. b**). Increasing selenization time not only increased the amount of Se but also separated the material into two separate phases CoS₂ and CoSe₂. The content of CoSe₂ also increased with time. But due to our inability to achieve pure phase CoSe₂, commercial CoSe₂ was used to compare the activity of other materials (**Fig. S6**). However, the activity of this commercial material was found to be extremely poor which can be attributed to the lack of active sites due to its bulk particles and lack of porosity.⁵¹

All electrochemical characteristics related to the HER of both meso-CoS₂ and meso-CoSSe-12h catalysts were measured using a three-electrode (rotating disc electrode, RDE) electrochemical cell having 0.5 M H₂SO₄ (aq.) solution (see **methods** section) as the electrolyte. A constant catalyst loading of 0.2 mg cm⁻² on the graphite electrode (having resistance below 10 ohms) was used to compare the activity of different catalysts. The overpotential (η) required to achieve a geometric current density of 10 mA cm⁻² was selected as the target parameter for their comparison and was measured by linear sweep voltammetry at a scan rate of 5 mV s⁻¹. The meso-CoSSe-12h catalyst achieved that (10 mA cm⁻²) current density at an overpotential (η) of -110 mV (versus the reversible hydrogen electrode, RHE) which was significantly lower (-358 mV vs. RHE) than that of the meso-CoS₂ catalyst (**Fig. 4. a, Table 1**). This activity was further compared to the reference electrode (Pt/ C), which required only ~35 mV (vs. RHE) of overpotential to reach to the 10 mA cm⁻² current density (**Fig. 4. a, Table 1**), under similar conditions. All data were *iR* corrected, and the ohmic losses of the system were always < 8 Ω . To know the kinetics of the process, Tafel slopes were calculated from the extrapolation of the linear region of overpotential versus log *J* plot, where a lower slope symbolizes faster kinetics. Consequently, the reaction kinetics of meso-CoSSe-12h (Tafel slope of 52 mV dec⁻¹) was found to be faster than the meso-CoS₂ (Tafel slope of 116 mV dec⁻¹ by) (**Fig. 4. b, Table 1**). The benchmark Pt/C displayed faster kinetics due to its lower Tafel slope value of 36 mV dec⁻¹ (see **Table S2** and **Table S3**). These values of the Tafel slope sug-

gested a possible Volmer-Heyrovsky pathway during the HER, where the electrochemical desorption of hydrogen (H) is the rate-determining step.²⁴ The intrinsic activity of active sites of a material is measured from the geometrical exchange current density at zero overpotential ($J_{0, geometrical}$). This activity is calculated from the intercept (at zero overpotential) of the fitting curve of the Tafel slope. Activities were 8 μ A cm⁻², 70 μ A cm⁻², and 890 μ A cm⁻² for meso-CoS₂, meso-CoSSe-12h, and Pt/C, respectively (**Note S6, Table 1**). A sharp ~9 fold increment of $J_{0, geometrical}$ for meso-CoSSe-12h as compared to the meso-CoS₂ revealed the enhancement of the intrinsic activity of meso-CoS₂ upon selenization. To understand more about the origin of this activity difference, their relative electrochemical surface areas were measured by extracting the double-layer capacitance (C_{dl}) using cyclic voltammetry (**Fig. 4. d**).²² This showed that the electrochemical surface area of meso-CoSSe-12h (38.25 cm²) was ~2 times higher than that of meso-CoS₂ (17.50 cm²). Therefore, we assume, due to this higher electrochemically active surface area (~2 times) and geometrical exchange current densities (~9 times), meso-CoSSe-12h exhibits better HER activity than meso-CoS₂. To determine the faradic efficiency of the meso-CoSSe-12h catalyst, hydrogen gas was produced and quantified at an interval of 20 minutes for 2 hours using a pre-determined calibration curve obtained from GC-TCD (**Fig. 4. e**). The experimental plot obtained from this process displayed ~99 % fit to the theoretical graph, confirming an accurate conversion of cathodic current to H₂ production.

To estimate the impact of Se doping in improving the activity of meso-CoS₂ in alkaline media (1 M KOH), the cathodic polarization curves of meso-CoSSe-12h and meso-CoS₂ catalysts were measured using linear sweep voltammetry (**Fig. S8. and Note S2**). This study showed a similar trend as for acidic media, confirming the drastic improvement of activity of meso-CoS₂ upon selenium (Se) doping. Moreover, excellent activities of meso-CoSSe-12h in both acidic and alkaline electrolytes distinguish this system from most metal sulfide systems such as CoS₂, MoS₂, and some metal phosphides (for example, Ni₂P), as they fail to perform under alkaline conditions.^{2,32}

To evaluate the stability of the meso-CoS₂-12h catalyst, an accelerated degradation study was performed under 0.5 M H₂SO₄ (aq.) solution as shown in (Fig. 5. a). The cathodic polarization curve obtained after 1,000 continuous cycles of voltammograms (scan rate: 50 mV s⁻¹) exhibited a negligible increase in η required to reach the current density of 100 mA cm⁻² as compared to its 1st polarization curve. Moreover, the catalyst was capable of generating this current density for at least 25 hours (Fig. 5. b). This indicates excellent stability of the meso-CoS₂-12h catalyst with acidic electrolyte. The unique design, the presence of earth-abundant elements (Co, S, and Se), excellent acid-base stability, and an outstanding HER performance of our

following methods mentioned in Note S8. The conjugate Histidine which is an amino acid was selected for its excellent complexation ability with both Co (II)^{54,55} and Co (III).⁵⁶ These strong tetrahedral complexes are expected to inhibit the cobalt species from participating in the HER process, which may help quantify the combined catalytic activity of sulfur and selenium. Similarly to block sulfur, the electrode catalyst was incubated with HAuCl₄·3H₂O, which is known to reduce the Au³⁺ species to Au clusters⁵⁷ over sulfur atoms.⁵⁸ This phenomenon is anticipated to measure the combined catalytic effect of cobalt and selenium. However, when both Histidine and HAuCl₄·3H₂O were used to incubating the catalyst, only selenium is expected to show catalytic activity.

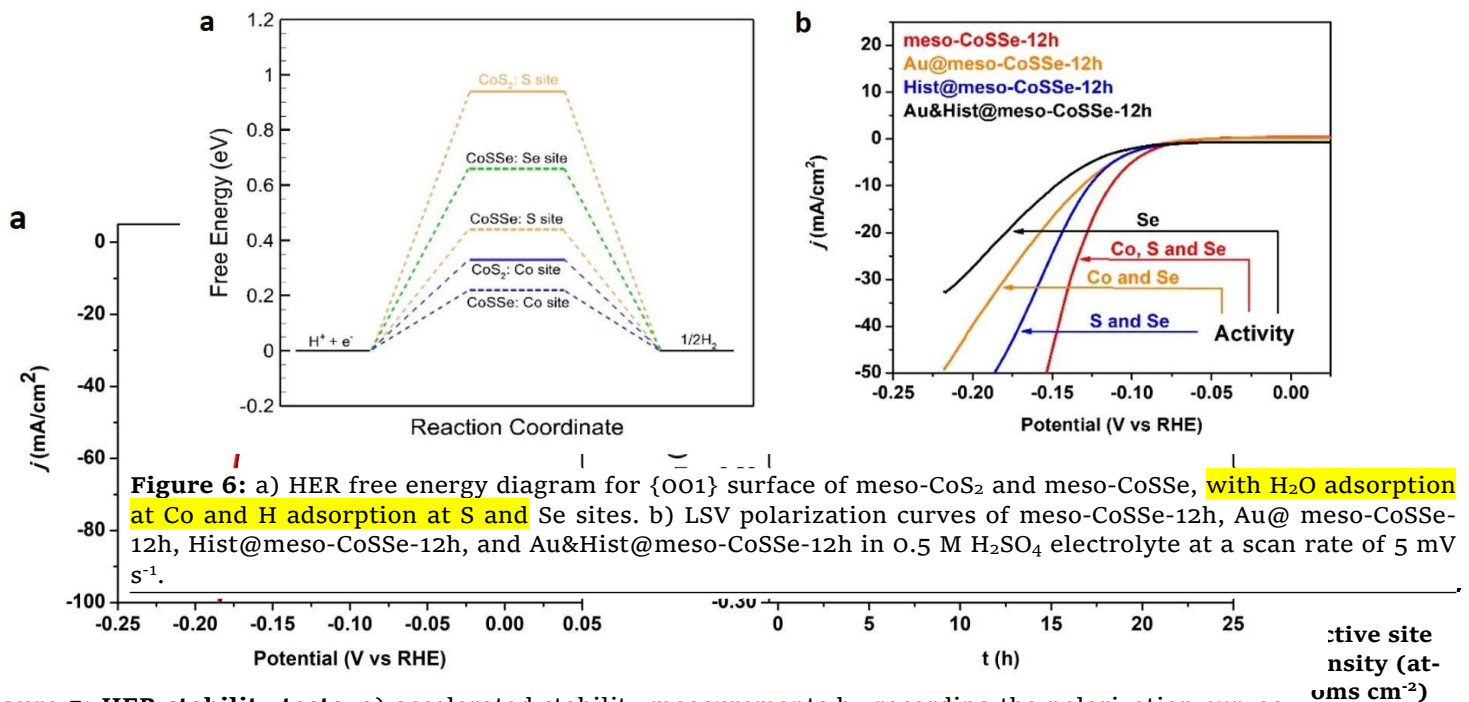


Figure 6: a) HER free energy diagram for {001} surface of meso-CoS₂ and meso-CoSSe, with H₂O adsorption at Co and H adsorption at S and Se sites. b) LSV polarization curves of meso-CoSSe-12h, Au@ meso-CoSSe-12h, Hist@meso-CoSSe-12h, and Au&Hist@meso-CoSSe-12h in 0.5 M H₂SO₄ electrolyte at a scan rate of 5 mV s⁻¹.

Figure 5: HER stability tests. a) accelerated stability measurements by recording the polarization curves for the meso-CoSSe-12h catalyst before and after 1,000 cyclic voltammograms at a scan rate of 50 mV s⁻¹ under acidic condition. b) The plot of η vs. time for the meso-CoSSe-12h catalyst at a constant cathodic current density of 100 mA cm⁻² under acidic condition.

pyrite-type material may have fundamental and applied importance, and is one of the best catalytic systems reported so far for HER.

To investigate the importance and contribution of each element of the catalyst, a few control experiments were performed. Individual active sites were blocked using specific reagents to measure the activity of remaining elements. HER polarization curves of these blocked materials were used to qualitatively estimate the role of individual active sites. To perform these experiments, three different electrodes were prepared

The polarization curves of these differently blocked catalysts were measured by linear sweep voltammetry (LSV) and compared with the previously acquired LSV of unblocked meso-CoSSe-12h catalyst (Fig. 6. b). Expectedly, the catalytic activity of all blocked electrodes was found to be lower than that of the unblocked one. Among these active site blocked electrodes, the cobalt-blocked electrode (Hist@meso-CoSSe-12h) exhibited the best activity, indicating a comparatively significant role of sulfur and selenium in the pro-

cess. Followed by this, the sulfur blocked electrode (Au@meso-CoSSe-12h) yielded a comparatively poor HER activity, which further declined for the sulfur and cobalt blocked electrode (Au&Hist@meso-CoSSe-12h) (**Fig. 6. b**). This signifies a comparatively higher contribution by the combined effect of Co-Se (Au@meso-CoSSe-12h) than the sole contribution of selenium of the system (Hist@meso-CoSSe-12h). This study identified S-Se to be most important, supporting our prior conclusion of newly developed super-active sulfur-selenium species (**Fig. 3. c**), in the CoSSe catalytic system.

DFT predicted lattice structures (**Fig. 1. b**) were used to identify the most stable planes where adsorption can occur. These data suggest that the 1S layer of (001) planes of both materials are the most stable (**Fig. 6. a**). As mentioned before, the adsorption of hydrogen is the most probable rate-determining step of this HER process. The determination of the free energy change of this step is very crucial. These free energies (ΔG_H) were calculated for all comparable surface sites. A reduction of free energy values for adsorption of hydrogen on both Co and S was seen in meso-CoSSe as compared to meso-CoS₂. Interestingly, a significant reduction of free energy was observed for sulfur (from 0.94 eV to 0.44 eV), as compared to the reduction on cobalt (from 0.33 eV to 0.22 eV). The free energy associated with the adsorption on Se was found to be 0.67 eV. This signifies the importance of Se in meso-CoSSe and validates its superior electrocatalytic HER activity over meso-CoS₂ as obtained experimentally. According to this DFT calculation, oxidation of Co sites was found to minimize the activation barrier, indicating faster kinetics for proton adsorption.

These studies inspired us to conduct a circuit model fitting analysis for electrochemical impedance spectroscopy (EIS) of both meso-CoS₂ and meso-CoSSe-12h materials to learn about their rates of charge transfer and electrochemically active interfaces (**Fig. S9**). This study revealed a decrease of ohmic resistance in meso-CoSSe-12h as compared to meso-CoS₂, enhancing the charge transfer by ~100 times (**Fig. S9**). However, the hemisphere obtained for meso-CoSSe-12h was significantly distorted as compared to that of meso-CoS₂. Therefore, to analyze them, we conducted simulation studies to generate equivalent circuits of experimentally obtained EIS spectra of both materials using various impedance elements (**Fig. S9**). This revealed the co-existence of charge transfer resistance (R_{ct}) and adsorption resistance (R_{ad}), for both cobalt and sulfur inter-

faces of meso-CoS₂, representing the manifestation of Volmer-Heyrovsky steps (**Fig. S9**).⁵⁹ Interestingly, selenization caused a sharp decrease of the resistivities of all pre-existing interfaces (cobalt and sulfur), besides the generation of another electrochemically active interface (**Fig. S9**). The agreement of this equivalent circuit with XPS studies confirm the development of a new sulfur-selenide species in meso-CoS₂ upon selenization (**Fig. 3. c**).

These newly generated active sites or interfaces increased the total turnover frequency (TOF) of the HER process due to the combined effect of its enhanced electrochemical surface area, exchange current density, and reaction kinetics (suggested by the lowering of Tafel slope). TOF indicates the number of gaseous hydrogen molecules generated at unit time (per second). Hence, TOF is considered to be the most critical characteristic of a catalyst which reveals its intrinsic catalytic efficiency. To quantify the TOF of these catalysts, the thermodynamic potential was calculated using the exchange current density (0 V vs. RHE). This yielded a TOF value of 3.34 H₂ s⁻¹ for meso-CoSSe-12h, which is approximately four times larger than the meso-CoS₂ (0.83 H₂ s⁻¹) (see detailed calculation in **Note S6**). Before this, we also calculated the electrochemically active surface area (**Note S5**), and the active site density (sites per cm²) (**Note S5, Table 1**) of both meso-CoS₂ and meso-CoSSe materials. Despite the reduction of active site density, the TOF of meso-CoSSe-12h increased as compared to meso-CoS₂ due to its higher (~9 times) intrinsic activity (**Note S6**) and electrochemically active surface area (ECSA).

In conclusion, we successfully designed a readily producible surface selenized mesoporous cobalt sulfide with excellent stability in acidic media. This enhanced the HER activity of the meso-CoS₂ catalyst drastically. We confirmed that the development of new terminal sulfur-selenium species, besides the oxidation of Co, was responsible for the enhanced HER activity of meso-CoSSe-12h. This resulted in a decrease of reaction overpotential (from 358 to 110 mV, vs. RHE); and an increase of the Tafel slope (from 116 to 52 mV dec⁻¹), intrinsic activity (geometrical exchange current density) (from 8 to 70 μ A cm⁻²) and turn over frequency (TOF) (from 0.83 to 3.34 H₂ s⁻¹) (**Figure 4**). These combined effects resulted in the enhanced HER activity. The reaction kinetics of these systems were also supported by DFT calculations. A similar trend of reactivity of this earth abundant transition metal dichalcogenide catalyst was shown in basic media. Besides its excellent

catalytic performance, outstanding stability (for at least 25 hours) and reusability (up to at least 1000 cycles), this system is fundamentally important for water splitting applications.

Methods

Materials Synthesis.

All chemicals were purchased from Sigma-Aldrich unless otherwise specified. Mesoporous-Co₃O₄, synthesized by a soft template mediated solvent evaporation induced self-assembly method,⁵² was sulfurized to produce mesoporous-CoS₂, which was selenized to produce the mesoporous-CoS_{Se} material.

Synthesis of meso-Co₃O₄

In a typical synthesis 0.02 mol of cobalt nitrate hexahydrate (Co(NO₃)₂·6H₂O) and 0.134 mol of 1-butanol were added to a 120 mL beaker. To this solution 0.00034 mol of poly(ethylene glycol)-block-poly(propylene glycol)-block-poly(ethylene glycol)(Pluronic P123, PEO₂₀PPO₇₀PEO₂₀, molar mass 5800 g mol⁻¹) and 0.032 mol of concentrated nitric acid (HNO₃) were added successively and stirred at room temperature until the solution became clear (purple). The resulting clear solution was then kept in an oven at 120°C for 4 hours to get a light pink dry powder. The product was collected and washed with excess ethanol, centrifuged, and dried in a vacuum oven overnight to get rid of excess surfactants and remaining organics. In the end, the dried pink powder was subjected to a heating cycle of 150°C for 12 h and then to 250°C for 4 hours. These steps are supposed to remove all surfactants and control the mesoporosity of the material.⁵²

Synthesis of meso-CoS₂

The black powder obtained from the previous step was then placed in the center of a standard 1.5-inch (diameter) quartz tube using a ceramic boat. Another ceramic boat containing sulfur was placed next to the first boat. The quartz tube was kept inside a tube-furnace and Helium (He) gas was used to purge the reactor for 30 minutes to remove air. Then 5 % H₂S was mixed on-line with 95 % of Helium to pass through the tube furnace with a feeding speed of 50 s.c.c.m. for 12 hours with a ramp rate of 1 °C/min up to 250 °C. The system was brought to room temperature before taking the sample out for further use.

Synthesis of meso-CoS_{Se}-*nh*.

The meso-CoS₂ powder obtained from the step mentioned above was placed in the center of a standard 1.5-inch (diameter) quartz tube (different than the one used for sulfurization to avoid contamination) using a ceramic boat. Another ceramic boat containing selenium was placed next to the first boat. The quartz tube was then kept inside a tube-furnace and Helium (He) gas was purged through the system for 30 minutes to remove air at a feeding speed of 50 s.c.c.m. Then, the temperature of the furnace was set to increase up to 250 °C for *n*th hours with a ramp rate of 1 °C/min. The furnace was allowed to cool down to room temperature to take the sample out for further use.

Characterization. A FEI Nova Nano SEM 450 was used to examine the sample morphology. A FEI Talos F200x TEM was used to observe the morphologic and structural characteristics of the samples. Chemical compositions and elemental oxidation states of the samples were investigated by XPS spectra, using a PHI 595 Multiprobe XPS. X-ray diffraction analysis was performed with a Rigaku Ultima IV-XRD (Rigaku Corporation). BET Surface area and BJH pore-size distribution of all synthesized materials were measured using a Quanta-chrome ASIQM 002-1 automated gas sorption analyzer. To analyze the Raman spectra of all reported materials, a Renishaw system 2000 was used at a wavelength of 514 nm. Rigaku ZSX Primus IV X-ray fluorescence was used for elemental analysis.

Electrochemical measurements. All electrochemical measurements were performed in a three-electrode setup using a CHI 760E workstation (US version). The catalyst was loaded on the working electrode (graphite electrode having a diameter of 0.48 cm) in the form of a gel (loading amount of the gel = 10 μL, mass loading of the catalyst 0.2 mg cm⁻²) to measure its electrochemical activity. The gel was made using 4 mg of the catalyst, 0.5 mg of Vulcan carbon, 40 μL of 5 wt % Nafion solution and 1mL of 1:1(v/v) water/ethanol (back ground current of Vulcan carbon was subtracted for all electrochemical experiments performed using it). The prepared mixture was sonicated for 1–2 h to get a nicely dispersed (Cole Parmer, model 08849-00) homogeneous suspension. The gel was dried after loading it on the electrode, prior to use. To select the counter electrode, a comparison between the Pt and the glassy carbon electrodes were performed which showed similar activity as the meso-CoS_{Se}-12h material in both cases (**Fig. S10. a**). A small enhancement in the activity in the presence of glassy carbon electrode

can be attributed to its higher surface area as compared to the platinum (Pt) electrode (**Fig. S10. a**). To ensure that the Pt counter did not dissolve or degrade during the hydrogen evolution reaction, SEM-EDX of the sample was measured after the 100th cycle of linear sweep voltammetry, which did not show the presence of Pt (**Fig. S10. c**). As a result, Pt wire was used as the counter electrode. The reference electrode was Hg/ HgCl₂/ KCl (sat) for measurements in 0.5 M H₂SO₄, and Ag/AgCl/ KCl (sat) for measurements in 1M KOH. Both of these two reference electrodes were calibrated against a reversible hydrogen electrode under the same testing conditions immediately before the catalytic characterization (**Fig. S11, and Note S7**). A scan rate of 5 mV s⁻¹ was used in the cyclic voltammograms of the HER activity unless otherwise noted. The electrolyte solution was purged with H₂ for 30 min before each test.

ASSOCIATED CONTENT

Supporting Information.

Determination of total energy change with increasing lattice strain; Raman; SEM, TEM; N₂ physisorption; GC-TCD signal of H₂; XPS calibration; Electrochemical performance of cobalt sulfoselenide materials from different calcination time, under alkaline electrolyte; CV of meso-CoS₂ and meso-CoSSe at different scan rates; Calibration of electrochemical instrument under acidic and alkaline medium; EIS Nyquist plot; Determination of counter electrode; elemental composition of meso-CoSSe materials derived from different calcination times; Comparison of electrochemical performance with previously reported materials; calculation of C_{dl}, ECSA, active site density, exchange current density, and TOF; Details of all calibration methods, active site blocking experiments, and computational method used to evaluate the observed catalytic activity.

AUTHOR INFORMATION

Corresponding Author

*steven.suib@uconn.edu.

AUTHOR CONTRIBUTIONS

*Biswanath Dutta and Yang Wu contributed equally to this work,

B.D. discovered the procedure, performed the syntheses. B.D. and Y.W. performed all electrochemical tests and part of the structural characterization. J.C. and J.W. performed all DFT calculations and dis-

cussed results with S.M.N. J.H. conducted TEM characterization. W.W. helped measuring X-ray photoelectric spectra. M.S. assisted in performing the active site blocking experiments. L.J. attained the Faradaic efficiency measurements. S.L.S. oversaw the whole project in all phases and provided constant suggestions throughout the research. B.D., Y.W., and S.L.S. analyzed all results and co-wrote the paper. All authors had an opportunity to comment on the manuscript.

ACKNOWLEDGMENT

S.L.S is grateful for the funding from the US Department of Energy, Office of Basic Energy Sciences, Division of Chemical, Biological and Geological Sciences under Grant DE-FG02-86ER13622.A000. We thank RIGAKU (USA) for XRF experiments. JFR thanks the Univ. of CT for an Academic Plan grant that partly supported this work. The SEM/TEM studies were performed using the facilities in the UConn/Thermo Fisher Scientific Center for Advanced Microscopy and Materials Analysis (CAMMA).

REFERENCES

- (1) Lewis, N. S.; Nocera, D. G. Powering the planet: chemical challenges in solar energy utilization. *Proc. Natl. Acad. Sci. U. S. A.* **2006**, *103*, 15729–15735.
- (2) Luo, J.; Im, J.-H.; Mayer, M. T.; Schreier, M.; Nazeeruddin, M. K.; Park, N.-G.; Tilley, S. D.; Fan, H. J.; Gratzel, M. Water photolysis at 12.3% efficiency via perovskite photovoltaics and Earth-abundant catalysts. *Science*. **2014**, *345*, 1593–1596.
- (3) Kyriakou, G.; Boucher, M. B.; Jewell, A. D.; Lewis, E. A.; Lawton, T. J.; Baber, A. E.; Tierney, H. L.; Flytzani-Stephanopoulos, M.; Sykes, E. C. H. Isolated Metal Atom Geometries as a Strategy for Selective Heterogeneous Hydrogenations. *Science*. **2012**, *335*, 1209–1212.
- (4) Hinnemann, B.; Moses, P. G.; Bonde, J.; Jørgensen, K. P.; Nielsen, J. H.; Horch, S.; Chorkendorff, I.; Nørskov, J. K. Biomimetic hydrogen evolution: MoS₂ nanoparticles as catalyst for hydrogen evolution. *J. Am. Chem. Soc.* **2005**, *127*, 5308–5309.
- (5) Turner, J. A. Sustainable Hydrogen Production. *Science*. **2004**, *305*, 972–974.
- (6) Faber, M. S.; Jin, S. Earth-abundant inorganic electrocatalysts and their nanostructures for energy conversion applications. *Energy Environ. Sci.* **2014**, *7*, 3519–3542.
- (7) Jin, H.; Wang, J.; Su, D.; Wei, Z.; Pang, Z.; Wang, Y. In situ Cobalt–Cobalt Oxide/N-Doped Carbon Hybrids As Superior Bifunctional Electrocatalysts for Hydrogen and Oxygen Evolution. *J. Am. Chem. Soc.* **2015**, *137*, 2688–2694.
- (8) Gong, M.; Zhou, W.; Tsai, M.-C.; Zhou, J.; Guan, M.; Lin, M.-C.; Zhang, B.; Hu, Y.; Wang, D.-Y.; Yang, J.; Pennycook, S. J.; Hwang, B.-J.; Dai, H. Nanoscale nickel oxide/nickel heterostructures for active

- hydrogen evolution electrocatalysis. *Nat. Commun.* **2014**, *5*, 4695.
- (9) Chen, W.-F.; Muckerman, J. T.; Fujita, E. Recent developments in transition metal carbides and nitrides as hydrogen evolution electrocatalysts. *Chem. Commun.* **2013**, *49*, 8896.
- (10) Lukowski, M. A.; Daniel, A. S.; Meng, F.; Forticaux, A.; Li, L.; Jin, S. Enhanced hydrogen evolution catalysis from chemically exfoliated metallic MoS₂ nanosheets. *J. Am. Chem. Soc.* **2013**, *135*, 10274-10277.
- (11) Benck, J. D.; Hellstern, T. R.; Kibsgaard, J.; Chakthranont, P.; Jaramillo, T. F. Catalyzing the hydrogen evolution reaction (HER) with molybdenum sulfide nanomaterials. *ACS Catalysis.* **2014**, *4*, 3957-3971.
- (12) Xie, J.; Zhang, J.; Li, S.; Grote, F.; Zhang, X.; Zhang, H.; Wang, R.; Lei, Y.; Pan, B.; Xie, Y. Controllable disorder engineering in oxygen-incorporated MoS₂ ultrathin nanosheets for efficient hydrogen evolution. *J. Am. Chem. Soc.* **2013**, *135*, 17881-17888.
- (13) Kibsgaard, J.; Chen, Z.; Reinecke, B. N.; Jaramillo, T. F. Engineering the surface structure of MoS₂ to preferentially expose active edge sites for electrocatalysis. *Nat. Mater.* **2012**, *11*, 963-969.
- (14) Li, D. J.; Maiti, U. N.; Lim, J.; Choi, D. S.; Lee, W. J.; Oh, Y.; Lee, G. Y.; Kim, S. O. Molybdenum sulfide/N-doped CNT forest hybrid catalysts for high-performance hydrogen evolution reaction. *Nano Lett.* **2014**, *14*, 1228-1233.
- (15) Voiry, D.; Salehi, M.; Silva, R.; Fujita, T.; Chen, M.; Asefa, T.; Shenoy, V. B.; Eda, G.; Chhowalla, M. Conducting MoS₂ nanosheets as catalysts for hydrogen evolution reaction. *Nano Lett.* **2013**, *13*, 6222-6227.
- (16) Benck, J. D.; Chen, Z.; Kuritzky, L. Y.; Forman, A. J.; Jaramillo, T. F. Amorphous molybdenum sulfide catalysts for electrochemical hydrogen production: Insights into the origin of their catalytic activity. *ACS Catal.* **2012**, *2*, 1916-1923.
- (17) Wang, H.; Lu, Z.; Kong, D.; Sun, J.; Hymel, T. M.; Cui, Y. Electrochemical tuning of MoS₂ nanoparticles on three-dimensional substrate for efficient hydrogen evolution. *ACS Nano* **2014**, *8*, 4940-4947.
- (18) Zhang, C.; Shi, Y.; Yu, Y.; Du, Y.; Zhang, B. Engineering Sulfur Defects, Atomic Thickness, and Porous Structures into Cobalt Sulfide Nanosheets for Efficient Electrocatalytic Alkaline Hydrogen Evolution. *ACS Catal.* **2018**, *8*, 8077-8083.
- (19) Voiry, D.; Yamaguchi, H.; Li, J.; Silva, R.; Alves, D. C. B.; Fujita, T.; Chen, M.; Asefa, T.; Shenoy, V. B.; Eda, G.; Chhowalla, M. Enhanced catalytic activity in strained chemically exfoliated WS₂ nanosheets for hydrogen evolution. *Nat. Mater.* **2013**, *12*, 850-855.
- (20) Lukowski, M. A.; Daniel, A. S.; English, C. R.; Meng, F.; Forticaux, A.; Hamers, R. J.; Jin, S. Highly active hydrogen evolution catalysis from metallic WS₂ nanosheets. *Energy Environ. Sci.* **2014**, *7*, 2608-2613.
- (21) Merki, D.; Fierro, S.; Vrabel, H.; Hu, X. Amorphous molybdenum sulfide films as catalysts for electrochemical hydrogen production in water. *Chem. Sci.* **2011**, *2*, 1262-1267.
- (22) Faber, M. S.; Dziejczak, R.; Lukowski, M. A.; Kaiser, N. S.; Ding, Q.; Jin, S. High-performance electrocatalysis using metallic cobalt pyrite (CoS₂) micro- and nanostructures. *J. Am. Chem. Soc.* **2014**, *136*, 10053-10061.
- (23) Kibsgaard, J.; Jaramillo, T. F.; Besenbacher, F. Building an appropriate active-site motif into a hydrogen-evolution catalyst with thiomolybdate [Mo₃S₁₃]²⁻ clusters. *Nat. Chem.* **2014**, *6*, 248-253.
- (24) Li, Y.; Wang, H.; Xie, L.; Liang, Y.; Hong, G.; Dai, H. MoS₂ nanoparticles grown on graphene: An advanced catalyst for the hydrogen evolution reaction. *J. Am. Chem. Soc.* **2011**, *133*, 7296-7299.
- (25) Tang, Y. J.; Wang, Y.; Wang, X. L.; Li, S. L.; Huang, W.; Dong, L. Z.; Liu, C. H.; Li, Y. F.; Lan, Y. Q. Molybdenum Disulfide/Nitrogen-Doped Reduced Graphene Oxide Nanocomposite with Enlarged Interlayer Spacing for Electrocatalytic Hydrogen Evolution. *Adv. Energy Mater.* **2016**, *6*, 1600116.
- (26) Xie, J.; Zhang, H.; Li, S.; Wang, R.; Sun, X.; Zhou, M.; Zhou, J.; Lou, X. W.; Xie, Y. Defect-rich MoS₂ ultrathin nanosheets with additional active edge sites for enhanced electrocatalytic hydrogen evolution. *Adv. Mater.* **2013**, *25*, 5807-5813.
- (27) Kong, D.; Wang, H.; Lu, Z.; Cui, Y. CoSe₂ nanoparticles grown on carbon fiber paper: An efficient and stable electrocatalyst for hydrogen evolution reaction. *J. Am. Chem. Soc.* **2014**, *136*, 4897-4900.
- (28) Zhou, H.; Yu, F.; Liu, Y.; Sun, J.; Zhu, Z.; He, R.; Bao, J.; Goddard III, W. A.; Chen, S.; Ren, Z. Outstanding hydrogen evolution reaction catalyzed by porous nickel diselenide electrocatalysts. *Energy Environ. Sci.* **2017**, *10*, 1-3.
- (29) Kong, D.; Wang, H.; Cha, J. J.; Pasta, M.; Koski, K. J.; Yao, J.; Cui, Y. Synthesis of MoS₂ and MoSe₂ films with vertically aligned layers. *Nano Lett.* **2013**, *13*, 1341-1347.
- (30) Wang, H.; Kong, D.; Johanes, P.; Cha, J. J.; Zheng, G.; Yan, K.; Liu, N.; Cui, Y. MoSe₂ and WSe₂ nanofilms with vertically aligned molecular layers on curved and rough surfaces. *Nano Lett.* **2013**, *13*, 3426-3433.
- (31) Yuan, S.; Deng, H.; Yang, X.; Hu, C.; Khan, J.; Ye, W.; Tang, J.; Song, H. Postsurface Selenization for High Performance Sb₂S₃ Planar Thin Film Solar Cells. *ACS Photonics* **2017**, *4*, 2862-2870.
- (32) Popczun, E. J.; Read, C. G.; Roske, C. W.; Lewis, N. S.; Schaak, R. E. Highly active electrocatalysis of the hydrogen evolution reaction by cobalt phosphide nanoparticles. *Angew. Chemie - Int. Ed.* **2014**, *53*, 5427-5430.
- (33) Liu, Q.; Tian, J.; Cui, W.; Jiang, P.; Cheng, N.; Asiri, A. M.; Sun, X. Carbon nanotubes decorated with CoP nanocrystals: A highly active non-noble-metal nanohybrid electrocatalyst for hydrogen evolution. *Angew. Chemie - Int. Ed.* **2014**, *53*, 6710-6714.
- (34) Popczun, E. J.; McKone, J. R.; Read, C. G.; Biacchi, A. J.; Wiltrout, A. M.; Lewis, N. S.; Schaak, R. E. Nanostructured nickel phosphide as an electrocatalyst for the hydrogen evolution reaction. *J. Am. Chem. Soc.* **2013**, *135*, 9267-9270.
- (35) Callejas, J. F.; McEnaney, J. M.; Read, C. G.; Crompton, J. C.; Biacchi, A. J.; Popczun, E. J.; Gordon, T. R.; Lewis, N. S.; Schaak, R. E. Electrocatalytic and photocatalytic hydrogen production from acidic and neutral-pH aqueous solutions using iron phosphide nanoparticles. *ACS*

- Nano* **2014**, *8*, 11101-11107.
- (36) Xiao, P.; Sk, M. A.; Thia, L.; Ge, X.; Lim, R. J.; Wang, J.-Y.; Lim, K. H.; Wang, X. Molybdenum phosphide as an efficient electrocatalyst for the hydrogen evolution reaction. *Energy Environ. Sci.* **2014**, *7*, 2624-2629.
- (37) Vrubel, H.; Hu, X. Molybdenum boride and carbide catalyze hydrogen evolution in both acidic and basic solutions. *Angew. Chemie - Int. Ed.* **2012**, *51*, 12703-12706.
- (38) Kibsgaard, J.; Jaramillo, T. F. Molybdenum phosphosulfide: An active, acid-stable, earth-abundant catalyst for the hydrogen evolution reaction. *Angew. Chemie - Int. Ed.* **2014**, *53*, 14433-14437.
- (39) Shifa, T. A.; Wang, F.; Liu, K.; Cheng, Z.; Xu, K.; Wang, Z.; Zhan, X.; Jiang, C.; He, J. Efficient Catalysis of Hydrogen Evolution Reaction from $WS_{2(1-x)}P_{2x}$ Nanoribbons. *Small* **2017**, *13*, 1603706.
- (40) Cabán-Acevedo, M.; Stone, M. L.; Schmidt, J. R.; Thomas, J. G.; Ding, Q.; Chang, H.-C.; Tsai, M.-L.; He, J.-H.; Jin, S. Efficient hydrogen evolution catalysis using ternary pyrite-type cobalt phosphosulphide. *Nat. Mater.* **2015**, *14*, 1245-1251.
- (41) Zhou, H.; Yu, F.; Huang, Y.; Sun, J.; Zhu, Z.; Nielsen, R. J.; He, R.; Bao, J.; Goddard III, W. A.; Chen, S.; Ren, Z. Efficient hydrogen evolution by ternary molybdenum sulfoselenide particles on self-standing porous nickel diselenide foam. *Nat. Commun.* **2016**, *7*, 12765.
- (42) McKone, J. R.; Sadtler, B. F.; Werlang, C. A.; Lewis, N. S.; Gray, H. B. Ni-Mo nanopowders for efficient electrochemical hydrogen evolution. *ACS Catal.* **2013**, *3*, 166-169.
- (43) Yu, Y.; Shi, Y.; Zhang, B. Synergetic Transformation of Solid Inorganic-Organic Hybrids into Advanced Nanomaterials for Catalytic Water Splitting. *Acc. Chem. Res.* **2018**, *51*, 1711-1721.
- (44) Ganesan, P.; Sivanantham, A.; Shanmugam, S. Inexpensive electrochemical synthesis of nickel iron sulphides on nickel foam: super active and ultra-durable electrocatalysts for alkaline electrolyte membrane water electrolysis. *J. Mater. Chem. A* **2016**, *4*, 16394-16402.
- (45) Vesborg, P. C. K.; Seger, B.; Chorkendorff, I. Recent development in hydrogen evolution reaction catalysts and their practical implementation. *J. Phys. Chem. Lett.* **2015**, *6*, 951-957.
- (46) Zou, S. X.; Zhang, Y.; Zou, X. As featured in: Featuring work from the research group of Noble metal-free hydrogen evolution catalysts for water splitting. *Chem. Soc. Rev.* **2015**, *44*, 5148-5180.
- (47) Kubas, G. J. Metal Dihydrogen and σ -Bond Complexes: Structure, Theory, and Reactivity, Kluwer Academic/Plenum Publishers, New York, **2001**, 1-16.
- (48) Wang, F.; Li, J.; Wang, F.; Shifa, T. A.; Cheng, Z.; Wang, Z.; Xu, K.; Zhan, X.; Wang, Q.; Huang, Y.; Jiang, C.; He, J. Enhanced Electrochemical H_2 Evolution by Few-Layered Metallic $WS_{2(1-x)}Se_{2x}$ Nanoribbons. *Adv. Funct. Mater.* **2015**, *25*, 6077-6083.
- (49) Wang, K.; Zhou, C.; Xi, D.; Shi, Z.; He, C.; Xia, H.; Liu, G.; Qiao, G. Component-controllable synthesis of $Co(S_xSe_{1-x})_2$ nanowires supported by carbon fiber paper as high-performance electrode for hydrogen evolution reaction. *Nano Energy* **2015**, *18*, 1-11.
- (50) Liu, K.; Wang, F.; Xu, K.; Shifa, T. A.; Cheng, Z.; Zhan, X.; He, J. $CoS_{2x}Se_{2(1-x)}$ nanowire array: an efficient ternary electrocatalyst for the hydrogen evolution reaction. *Nanoscale* **2016**, *8*, 4699-4704.
- (51) Sun, T.; Xu, L.; Yan, Y.; Zakhidov, A. A.; Baughman, R. H.; Chen, J. Ordered Mesoporous Nickel Sphere Arrays for Highly Efficient Electrocatalytic Water Oxidation. *ACS Catal.* **2016**, *6*, 1446-1450.
- (52) Poyraz, A. S.; Kuo, C.-H.; Biswas, S.; King'ondo, C. K.; Suib, S. L. A general approach to crystalline and monomodal pore size mesoporous materials. *Nat. Commun.* **2013**, *4*, 1-10.
- (53) Lyapin, S. G.; Utyuzh, A. N.; Petrova, A. E.; Novikov, A. P.; Lograsso, T. A.; Stishov, S. M. Raman studies of nearly half-metallic ferromagnetic CoS_2 . *J. Phys. Condens. Matter* **2014**, *26*, 396001.
- (54) Morris, P. J.; Martin, R. B. Tetrahedral Complexes of Cobalt (II) with L-Histidine, Histamine, Imidazole, and N-Acetyl-L-histidine. *J. Am. Chem. Soc.* **1970**, *92*, 1543-1546.
- (55) Greiner, B. A.; Marshall, N. M.; Narducci Sarjeant, A. A.; McLauchlan, C. C. Imidazole-based nickel(II) and cobalt(II) coordination complexes for potential use as models for histidine containing metalloproteins. *Inorganica Chim. Acta* **2007**, *360*, 3132-3140.
- (56) Louie, A. Y.; Meade, T. J. A cobalt complex that selectively disrupts the structure and function of zinc fingers. *Proc. Natl. Acad. Sci. U. S. A.* **1998**, *95*, 6663-6668.
- (57) Häkkinen, H. The gold-sulfur interface at the nanoscale. *Nat. Chem.* **2012**, *4*, 443-455.
- (58) Lengke, M. F.; Ravel, B.; Fleet, M. E.; Wanger, G.; Gordon, R. A.; Southam, G. Mechanisms of gold bioaccumulation by filamentous cyanobacteria from gold(III)-chloride complex. *Environ. Sci. Technol.* **2006**, *40*, 6304-6309.
- (59) Armstrong, R. D.; Henderson, M. J. Impedance plane display of a reaction with an adsorbed intermediate. *Electroanal. Chem. Interfacial Electrochem.* **1972**, *39*, 81-90. Benck, J. D.; Chen, Z.; Kuritzky, L. Y.; Forman, A. J.; Jaramillo, T. F. *ACS Catal.* **2012**, *2*, 1916-1923.

